39th AIAA/ASME/SAE/ASEE Joint Propulsion Conference and Exhibit
20-23 July 2003, Huntsville, Alabama

AIAA 2003-5206

LES of Multiple Jets in Crossflow using a Coupled Lattice Boltzmann-Finite Volume Solver

H. Feiz and S. Menon
School of Aerospace Engineering
Georgia Inst. of Technology
Atlanta, Georgia, USA 30332

39th AIAA/ASME/SAE/ASEE Joint Propulsion Conference 20-23 July 2003 / Huntsville, AL

For permission to copy or republish, contact the American Institute of Aeronautics and Astronautics 1801 Alexander Bell Drive, Suite 500, Reston, VA 22191–4344

Copyright © 2003 by Feiz and Menon. Published by the American Institute of Aeronautics and Astronautics, Inc., with permission.

LES of Multiple Jets in Crossflow using a Coupled Lattice Boltzmann-Finite Volume Solver

H. Feiz* and S. Menon†
School of Aerospace Engineering
Georgia Inst. of Technology
Atlanta, Georgia, USA 30332

Three dimensional large-eddy simulations (LES) of single and multiple jet-in-cross-flow (JICF) are conducted using the 19-bit Lattice Boltzmann Equation (LBE) method coupled with a conventional finite-volume (FV) scheme. In this coupled LBE-FV approach, the LBE-LES is employed to simulate the flow inside the jet nozzles while the FV-LES is used to simulate the crossflow. The key application area is to study the micro blowing technique (MBT) for drag control similar to the recent experiments at NASA/GRC. It is necessary to resolve the flow inside the micro-blowing and suction holes with high resolution without being restricted by the FV time-step. The coupled LBE-FV-LES approach achieves this objectives in a computationally efficient manner. A single jet in crossflow case is used for validation purpose and the results are compared with experimental data and full LBE-LES simulation. Good agreement with data is obtained. Subsequently, MBT over a flat plate with porosity of 25% is simulated using 9 jets in a compressible cross flow at a Mach number of 0.4. Two cases with injection ratios of 0.02 and 0.07 are conducted to investigate how the blowing rate impacts skin friction. It is shown that MBT suppresses the near-wall vortices and reduces the skin friction by up to 50 percent. This is in good agreement with experimental data.

1 Introduction

In recent years, a novel drag reduction method in turbulent boundary layers has been demonstrated using a micro-blowing technique (MBT) at NASA GRC.[1,2,3,4,5] Key features of this technique (in contrast to earlier more conventional blowing method) are the low effective roughness for the porous skin (achieved due to the use of micro holes) and the minimal amount of injection flow rate needed to achieve drag control. Results under laboratory and full-scale operating conditions show that significant skin friction drag reduction (as much as 50-70 percent) can be achieved using MBT. MBT appears to show even higher drag reduction in supersonic boundary layers with an added advantage of reduction of noise.

Interesting observations in subsonic flow are that the drag can be controlled by adjusting the injection flow rate and that the maximum drag reduction appears to occur within regions of adverse pressure gradient. However, more recent results in strongly adverse pressure gradient flow on a strut suggest that micro-blowing can lead to increased boundary layer and wake thickness[5] which can result in an increase in pressure drag for external flows. Thus, there are still many unresolved questions regarding the underlying physics of drag reduction as achieved by the MBT and how this blowing process impacts the large-scale flow features. Furthermore, the experimental data suggests that the injection system (and the injected airflow) couple strongly with the outer (primary) flow especially in adverse pressure gradient flow. This makes the optimization of the design of this device problematic, and parametric study using primarily an experimental approach is not a cost-effective approach.

Numerical studies of the MBT in subsonic turbulent boundary layers have also been recently reported[6] in which a steady-state 3D code was used. Only a very few micro holes and the cross-stream boundary layer were numerically modeled using a low Reynolds number turbulence closure. Results showed that for all the simulated cases, micro-blowing leads to unsteadiness due to the formation of vortices. However, due to the steady-state model employed this feature could not be studied.

MBT studies using unsteady simulation is problematic since many holes (typically hundreds) have to be simulated simultaneously in order to resolve the dynamics. Moreover, to properly capture this dynamics, the flow inside the holes has to be computed so that the flow at the hole exit planes evolve naturally (the flow can be blowing or suction depending upon the local pressure gradient). This type of requirement implies a

*Student Member, AIAA
†Professor, Associate Fellow, AIAA

Copyright © 2003 by Feiz and Menon. Published by the American Institute of Aeronautics and Astronautics, Inc. with permission.

very high computational overhead due to the increased resolution, and also due to the reduced time-step if a conventional FV scheme is employed. Clearly, an alternate technique is needed if this type of flow physics has to be simulated.

In the past, MBT studies in supersonic boundary layers were conducted[7] in which Micro-Electro-Mechanical System (MEMS) based micro-scale blowing/suction devices were simulated using direct numerical simulation (DNS) in 2D. Significant unsteadiness is shown to be associated with the interaction between the injected fluid and the supersonic boundary layer. Vortex shedding and even pairing occurs in the near field of the injected fluid in the boundary layer. By combining blowing and suction it was further shown that not only drag can be reduced but also that it can be increased at specific location.

It is clear that DNS of 3D high Reynolds number turbulent boundary layer with proper resolution of the micro holes is beyond the current and perhaps future computational capability. An alternate method that has the potential for such a study is based on large-eddy simulations (LES). In LES, all scales larger than the grid are resolved in a space and time accurate manner and only the scales smaller than the grid are modeled using a subgrid model. Although LES looks promising, it also has a serious problem in near-wall flows. To properly resolve the small-scale dynamics in the log layer, the wall normal resolution has to be close to the DNS requirement. This implies that the computational cost will be unacceptable. Clearly, an alternate method is required and more recently, a method based on two-scale decomposition called Two-Level Simulation (TLS) has been developed[8] to address this particular issue. In TLS, the small-scale field is simulated on a finer resolution grid that is embedded inside the conventional LES grid. Although this method has the potential for dealing with near-wall physics, extending this approach to deal with the flow inside the micro holes still remains to be addressed.

Here, we consider another approach that has the potential for dealing with the flow inside and outside the micro holes. In this approach, we combine a LBE-LES method with the conventional FV-LES method to achieve proper resolution in both regions. 2D and 3D LBE-LES methods have been demonstrated for fuel-air mixing and jet in crossflow in the past.[9,10] In all these reported studies, the flow inside the injector or jet inlet is resolved completely using LBE and the flow at the exit plane evolves in a natural manner. The unique feature of the LBE approach is that it solves the Boltzmann equation (which, in the continuum limit recovers the Navier-Stokes equation). Since the Boltzmann equation is a single scalar equation, it is computationally very efficient (in fact, orders of magnitude faster than conventional FV algorithm). Thus, very high resolution (in fact, DNS-like resolution) can be use in the LBE model without a significant increase in the computational cost. In the present study, the LBE model is employed primarily to resolve the flow field inside the injectors while the conventional FV-LES model is used to simulate the boundary layer flow. This approach takes the best of both worlds and couples them together within a single formulation. The LBE solver is fully coupled to the LES solver and interacts across block structured grid domains. Thus, in the injection port regions and in the near-wall region (e.g., below y+ = 100), a high (DNS-like) resolution can be used, and the flow field simulated without requiring any modeling using the LBE model, while in regions away from the wall, a conventional FV LES code can be employed.

This paper reports on the first fully coupled LBE-LES and FV-LES simulation of turbulent jet in crossflow and multiple micro-jets in crossflow. Earlier the single jet in crossflow (JICF) was simulated using a LBE-LES method[10] and compared to experimental data. Very good agreement was obtained. Here, we simulate the same test case using the coupled formulation and compare to earlier studies to demonstrate the applicability of this coupled method. Subsequently, the coupled solver is used to simulate a matrix of 3 x 3 micro holes in a high Mach number turbulent boundary layer. This test case is similar to the experiment at NASA/GRC[4] except that only a 3 x 3 matrix is simulated, whereas in the experiment, thousands of micro holes on a large flat plate were employed. Our present effort is to demonstrate this coupled approach and eventually we will consider methods to extend this technique to handle many holes simultaneously.

2 Simulation Model

The simulation model for the finite-volume and lattice approaches are summarized here for completeness. More details are given in the cited references.

2.1 FV-LES Formulation

Our interest here is the application of MBT to reduce skin friction drag on aircraft wings under realistic flight conditions in the Mach number range of 0.4 - 1.8. Therefore, we employ a fully compressible Navier-Stokes solver that has been used extensively in the past and is fully validated in non-reacting[11,12] and reacting flows.[13,14,15] The solver is nominally second-order accurate in both space and time; however, it also has the option for fourth order accuracy in space.

The LES equations are obtained by the application of a spatial filter to the governing equations of motion. For the compressible equations, a Favre spatial filter is employed to separate the resolved and unresolved motion.[16] For a finite-volume scheme, a low-pass, top-hat filter of the local grid size ($\overline{\Delta}$) is appropriate. The filtering operation results in the compressible LES

equations (details are avoided here for brevity).

The sub-grid terms resulting from the filtering operation, denoted with super-script ^{sgs}, represent the effect of small-scale motion upon the resolved-scales in the form of additional stresses and fluxes. The filtered velocity, $\widetilde{u}_i$, and temperature, $\widetilde{T}$, are used to approximate the filtered viscous shear stress, $\overline{\tau}_{ij}$ and the filtered heat conduction $\overline{q}_i$, respectively. The subgrid stress tensor, subgrid heat flux, and unresolved viscous work are defined, respectively, formally as:

$$\begin{aligned} \tau_{ij}^{sgs} &= \overline{\rho}[\widetilde{u_i u_j} - \widetilde{u}_i \widetilde{u}_j] \\ H_i^{sgs} &= \overline{\rho}[\widetilde{E u_i} - \widetilde{E}\widetilde{u}_i] + [\overline{p u_i} - \overline{p}\widetilde{u}_i] \\ \sigma_i^{sgs} &= [\overline{u_j \tau_{ij}} - \widetilde{u}_j \overline{\tau}_{ij}]. \end{aligned} \tag{1}$$

The subgrid terms, Eq. 1, require explicit modelling since the small-scale correlations are not known. Since, dissipation of the turbulent kinetic energy occurs primarily in the small-scales, an eddy viscosity ν_t model is employed. The simplest model is: $\nu_t = C_\nu l^{sgs} v^{sgs}$, where l^{sgs} and v^{sgs} are respectively, the characteristic length and velocity scale at the small-scale, and C_ν is a coefficient of proportionality. For LES, characteristic length scale is modelled as the local grid size, $\overline{\Delta}$ $(= (\Delta x_1 \Delta x_2 \Delta x_3)^{1/3})$. The velocity scale is obtained by solving a transport model for the subgrid kinetic energy[17] in which $v^{sgs} = \sqrt{k^{sgs}}$, where k^{sgs} is the subgrid kinetic energy. Past studies have demonstrated that since the algebraic model requires equilibrium between production and dissipation of energy (which occurs only in the dissipation region of the spectra), the grid resolution requirement can be quite severe, especially for the near-wall problem. Here, we employ the k^{sgs} based subgrid closure which has a significant advantage over the algebraic model since equilibrium between production and dissipation is not needed, and as a result, the grid scale cutoff can be in the inertial range. This ability allows the use of the k^{sgs} subgrid closure to simulate high-Re flows using relative coarse grids, shown in many past studies.[18,14,11]

A transport equation for the subgrid kinetic energy, defined as $k^{sgs} = \frac{1}{2}[\widetilde{u_k^2} - \widetilde{u}_k^2]$ is:[19,18,20]

$$\frac{\partial \overline{\rho}\, k^{sgs}}{\partial t} + \frac{\partial}{\partial x_i}(\overline{\rho}\, \widetilde{u}_i k^{sgs}) = P^{sgs} - D^{sgs} + \frac{\partial}{\partial x_i}\left(\overline{\rho}\, \frac{\nu_t}{Pr_t} \frac{\partial k^{sgs}}{\partial x_i}\right) \tag{2}$$

were Pr_t is the turbulent Prandtl number which is assumed constant and equal to unity. Here, P^{sgs} and D^{sgs} are, respectively, the production and dissipation of k^{sgs}. The production term is defined as, $P^{sgs} = -\tau_{ij}^{sgs}(\partial \widetilde{u}_i / \partial x_j)$, where τ_{ij}^{sgs} is the modelled subgrid stress tensor,

$$\tau_{ij}^{sgs} = -2\overline{\rho}\, \nu_t (\widetilde{S}_{ij} - \frac{1}{3}\widetilde{S}_{kk}\delta_{ij}) + \frac{2}{3}\overline{\rho} k^{sgs}\delta_{ij}, \tag{3}$$

In the above expression, $\nu_t = C_\nu (k^{sgs})^{1/2}\overline{\Delta}$ and $\widetilde{S}_{ij}, = \frac{1}{2}(\partial \widetilde{u}_i/\partial x_j + \partial \widetilde{u}_j/\partial x_i)$ is the resolved rate-of-strain tensor. The dissipation term is modelled as $D^{sgs} = C_\varepsilon \overline{\rho}(k^{sgs})^{3/2}/\overline{\Delta}$.

There are two coefficients in this model, C_ν and C_ε that have to be either specified or determined dynamically as part of the solution. In the present study, we employ the aforementioned LDKM model to obtain these coefficients locally as a function of space and time. Although the LDKM model has been discussed in detail elsewhere,[19,18,13] for completeness, we summarize the key features of this model.

Experimental measurements in high Re turbulent jet[21] suggest that the subgrid stress τ_{ij}^{sgs} at the grid filter level $\overline{\Delta}$ and the Leonard's stress L_{ij} at the test filter level $\widehat{\Delta}(= 2\overline{\Delta})$ are self-similar. In the LDKM model, this observation is extended and it is assumed that L_{ij} and the subgrid stress $\widehat{\tau}_{ij}^{sgs}$ at the test filter level are also similar. Using this, $\widehat{\tau}_{ij}^{sgs}$ is modeled using the same form as for τ_{ij}^{sgs} (Eq. 3), except that all variables are defined at the test filter level. Thus, for example, the subgrid kinetic energy at the test filter level is $k_{test} = \frac{1}{2}[\widehat{\widetilde{u_k}^2} - \widehat{\widetilde{u}_k}^2]$ and this quantity is fully resolved at the test filter $\widehat{\Delta}$ level. Thus, a direct (but over determined) expression for the model coefficient C_ν is obtained:

$$C_\nu = \frac{L'_{ij} M_{ij}}{2 M_{ij} M_{ij}} \tag{4}$$

Here, a least-square method is employed to obtain C_ν. In the above expression

$$L'_{ij} = L_{ij} - \frac{2}{3}\widehat{\overline{\rho}}\; k_{test}\delta_{ij} \tag{5}$$

$$L_{ij} = -2\widehat{\overline{\rho}} C_\nu \sqrt{k_{test}}\widehat{\Delta}(\langle \tilde{S}_{ij}\rangle - \frac{1}{3}\langle \tilde{S}_{ij}\rangle \delta_{ij}) + \frac{2}{3}\widehat{\overline{\rho}}\; k_{test}\delta_{ij} \tag{6}$$

$$M_{ij} = -\widehat{\overline{\rho}}\; \sqrt{k_{test}}\widehat{\Delta}(\langle \tilde{S}_{ij}\rangle - \frac{1}{3}\langle \tilde{S}_{ij}\rangle \delta_{ij}) \tag{7}$$

A similar approach is used to obtain the dissipation coefficient C_ε such that:

$$C_\epsilon = \frac{\widehat{\Delta}\mu'}{\widehat{\overline{\rho}}\; k_{test}^{3/2}}(\langle \tau_{ij}^{sgs} \frac{\partial u_i}{\partial x_j}\rangle - \langle \overline{\tau}_{ij}^{sgs}\rangle \langle \frac{\partial u_i}{\partial x_j}\rangle) \tag{8}$$

In the above formulation $< f >$ and $\widehat{f}$ both indicate test filtering. More details are given elsewhere.[19,18] There are a few noteworthy points to highlight in the LDKM closure: (a) the LDKM approach does not employ the Germano's identity,[22] (b) the self-similar approach implies that both $\overline{\Delta}$ and $\widehat{\Delta}$ must lie in the inertial range and this provides an estimate for the minimum grid resolution that can be used for a given Re, (c) the denominator in both Eqns. 4 and 8 are

well-defined quantities at the test filter level and can be directly computed, (d) the evaluation of the coefficients can be carried out locally (i.e., at all grid points) in space without encountering instability, (e) the LDKM approach satisfies all the realizability conditions[23] in majority of the grid points even in complex flows, and (f) the dynamic evaluation can be used near walls without any change. Finally, the computational overhead of the LDKM is not very significant since only one additional equation has to be solved.

2.2 LBE-LES Formulation

The LBE method originates from a Boolean fluid model known as the lattice gas automata (LGA) which simulates viscous fluid flow by tracing the fluid motion through advection of fluid particles and particle collision on a regular lattice. LBE is an improvement over LGA in which the Boolean fluid model is replaced by a single continuous particle distribution, which is analogous to the particle distribution function in kinetic theory. This replacement eliminates the intrinsic noise inherent in LGA schemes and overcomes the shortcomings of a limited transport coefficient. The introduction of the BGK single relaxation time model for the collision operator further simplifies the algorithm and eliminates the lack of Galilean invariance and the dependence of pressure on velocity.[24, 25] This model assumes that the particle distribution function relaxes to its equilibrium state at a constant rate, and the collision operator is similar to the classical BGK Boltzmann operator.[26]

Whereas conventional Navier-Stokes schemes solve the macroscopic properties of the fluid explicitly, LBE method solves the Boltzmann equation by tracking the evolution of the microscopic particle distribution of the fluid in phase space (velocity space, physical space and time). Consequently, the conserved variables of the fluid (density and momentum) are obtained indirectly by local integration of the particle distribution (over the velocity space). The incompressible Navier-Stokes is recovered in the nearly incompressible limit of LBE using the Chapman-Enskog expansion. For the present MBT application this is an acceptable model since we are interest in using the LBE approach only within the jet injectors where the flow is at a very low speed.

Solving the lattice Boltzmann equation instead of the Navier-Stokes equation provides three distinct advantages. First, due to the kinetic nature of the LBE method, the convection operator is linear. Simple convection in conjunction with a collision process allows the recovery of the nonlinear macroscopic advection through multi-scale expansions. Second, because the macroscopic properties of the flow field is not solved directly, LBE method avoids solving the Poisson equation, which proves to be numerically difficult in most finite difference methods. Third, the macroscopic properties are obtained from the microscopic particle distributions through simple arithmetic integration. More details are given in a recent review.[27]

LBE method consists of two primary steps. The particles first stream to its next nearest neighbor in the direction of its prescribed velocity. Subsequently, particles of different velocities arriving at the same node interacts with each other by relaxing to its local equilibrium values which are formulated specifically to recover the low Mach number limit of the Navier-Stokes equation. The evolution of the non-dimensional distribution function f_α is thus governed by:

$$f_\alpha(\mathbf{x} + \mathbf{e}_\alpha\delta, t + \delta) - f_\alpha(\mathbf{x}, t) = \frac{1}{\tau}[f_\alpha^{eq}(\mathbf{x}, t) - f_\alpha(\mathbf{x}, t)],$$

$$\alpha = 0, 1, \cdots, 18 \tag{9}$$

where τ is the relaxation time, f_α^{eq} is the equilibrium distribution function and e_α is the particle speed in α direction. The characteristic speed is thus $c = \mathbf{e}_\alpha\delta/\delta = |\mathbf{e}_\alpha|$. Rest particles of type 0 with $e_0 = 0$ are also allowed. Note that the time step and the lattice spacing each have equal spacing of unity. Thus, $\delta = 1$. More recently, studies have demonstrated that multiple relaxation time models can be developed when one needs to simulate scalar mixing at different Schmidt number.[28]

In principle, there are an infinite number of possible velocity directions in the 3D velocity space. Discretizing these infinite number of velocity directions into a fixed set of velocity directions inevitably introduces discretization errors to the solution. As a general rule, the accuracy of the model to simulate Navier-Stokes flow comes at the expense of increasing computational cost resulting from the number of discrete velocities used in the model. Frisch et al.[29] have shown that the Navier-Stokes equation cannot be recovered unless sufficient discrete velocities is used to ensure lattice symmetry.

There are various 3D cubic lattice models developed, most notably the 15-bit (D315), 19-bit (D3Q19), and 27-bit (D3Q27) model.[30] Here, using common notations in scientific literatures, D is the number of dimensions and Q is the number of discrete velocities. A variant model can be derived from each model by removing the rest particle, resulting in models D3Q14, D3Q18, and D3Q26. There models are used less frequently because LBE models with a rest velocity generally have better computational stability. In previous numerical simulations of a square duct, a lid-driven cavity and a circular pipe,[31] no significant improvement in accuracy is observed when the D3Q27 model was used over the D3Q19 model, and thus, the D3Q19 model is assumed to be sufficiently accurate for the current purpose.

The 19-bit velocity field (Fig.1) is:

$$\mathbf{e}_\alpha = \begin{cases} (0,0,0) \\ \text{for } \alpha = 0, \text{ rest particle,} \\ ((\pm 1,0,0),(0,\pm 1,0),(0,0,\pm 1))c \\ \text{for } \alpha = 1,2,\cdots,6, \text{ class I links,} \\ ((\pm 1,\pm 1,0),(0,\pm 1,\pm 1),(\pm 1,0,\pm 1))\sqrt{2}c \\ \text{for } \alpha = 7,8,\cdots,18, \text{ class II links.} \end{cases} \tag{10}$$

Here, f_α^{eq} is given by the following form:

$$f_\alpha^{eq} = w_\alpha \rho [1 + \frac{3(\mathbf{e}_\alpha \cdot \mathbf{u})}{c^2} + \frac{9}{2}\frac{(\mathbf{e}_\alpha \cdot \mathbf{u})^2}{c^4} - \frac{3}{2}\frac{\mathbf{u}^2}{c^2}], \tag{11}$$

where

$$w_\alpha = \begin{cases} \frac{1}{3} & \alpha = 0 \\ \frac{1}{18} & \alpha = 1,2,\cdots,6 \\ \frac{1}{36} & \alpha = 7,8,\cdots,18. \end{cases}$$

The macroscopic properties of the flow field can be obtained by integrating the distribution functions over the velocity space:

$$\rho = \sum_\alpha f_\alpha \tag{12}$$

$$\rho \mathbf{u} = \sum_\alpha \mathbf{e}_\alpha f_\alpha, \qquad \alpha = 0,1,...,18 \tag{13}$$

where ρ is the density and $\mathbf{u}$ is the velocity. All macroscopic properties are obtained as function of space and time from this integration.

The Navier-Stokes mass and momentum equations are obtained by using the BGK single relaxation time model,[26] and by employing Chapman-Enskog expansion are:

$$\frac{\partial \rho}{\partial t} + \frac{\partial \rho u_i}{\partial x_i} = 0 \tag{14}$$

$$\frac{\partial(\rho\, u_i)}{\partial t} + \frac{\partial \rho u_i u_j}{\partial x_j} = \frac{\partial (c_s^2 \rho)}{\partial x_i} + \frac{\partial 2\nu\rho S_{ij}}{\partial x_j} \tag{15}$$

Here, repeated indices indicate summation and $S_{ij} = \frac{1}{2}(\partial \tilde{u}_i/\partial x_j + \partial \tilde{u}_j/\partial x_i)$ is the strain-rate tensor. The non-dimensional pressure is given by the constant temperature ideal gas equation of state $p = c_s^2 \rho$ where c_s is the speed of sound with ($c_s = c/\sqrt{3}$), and $\nu = [(2\tau - 1)/6]$ is the kinematic viscosity.

For LES application we consider the filtered distribution function such that the LBE-LES form of the governing equation is

$$\bar{f}_\alpha(\mathbf{x} + \mathbf{e}_\alpha \delta, t + \delta) - \bar{f}_\alpha(\mathbf{x}, t) = \frac{1}{\tau_{sgs}}[\bar{f}_\alpha^{eq}(\mathbf{x}, t) - \bar{f}_\alpha(\mathbf{x}, t)]$$

$$\alpha = 0,1,\cdots,18 \tag{16}$$

where the distribution function $\bar{f}_\alpha$ represents only those of the resolved scales. The effect of the unresolved scale motion is modelled through an effective collision term, which in the BGK approximation is included as an effective relaxation time τ_{sgs}. The form of the subgrid correction is not fully explored at present. In conventional LES, models based on the one-equation model for the subgrid kinetic energy[32] have proven quite robust and therefore, a similar approach is being explored here.

In the earlier studies[10] the effective relaxation time was obtained using an eddy viscosity model (based on the Smagorinsky's eddy viscosity model) such that:

$$\nu + \nu_\tau = \frac{2\tau_{sgs} - 1}{6} \tag{17}$$

with the eddy viscosity ν_τ determined using:

$$\nu_\tau = C_\nu \overline{\Delta}^2 S \tag{18}$$

where C_ν is the Smagorinsky constant, $\overline{\Delta} = (\Delta_x \Delta_y \Delta_z)^{\frac{1}{3}}$ is the associated length scale and $S = |\bar{S}_{ij}\bar{S}_{ij}|$. Here, $\bar{S}_{ij} = \frac{1}{2}(\partial \bar{u}_i/\partial x_j + \partial \bar{u}_j/\partial x_i)$ is the resolved-scale rate-of-strain tensor is the characteristic filtered rate of strain tensor.

The Smagorinsky constant C_ν is determined using the localized dynamic model (LDM)[32,18] described earlier. Thus, C_ν is obtained using

$$C_\nu = \frac{L'_{ij} M_{ij}}{2 M_{ij} M_{ij}} \tag{19}$$

where $L'_{ij} = L_{ij} - \frac{2}{3}\widehat{\bar{\rho}} k^{test} \delta_{ij}$ and $M_{ij} = -\widehat{\bar{\rho}}\sqrt{k^{test}}\widehat{\Delta}(\langle \tilde{S_{ij}} \rangle - \frac{1}{3}\langle \tilde{S_{kk}} \rangle \delta_{ij})$. Here, $L_{ij} = \widehat{\bar{\rho}}(\langle \tilde{u_i}\tilde{u_j} \rangle - \langle \tilde{u_i} \rangle \langle \tilde{u_j} \rangle)$ is the Leonard stress tensor and $k^{test} = \frac{1}{2}(\langle \tilde{u_i}\tilde{u_j} \rangle - \langle \tilde{u_i} \rangle \langle \tilde{u_j} \rangle) = \frac{1}{2} L_{kk}/\widehat{\bar{\rho}}$ is the resolved kinetic energy at the test-filter level.

This algebraic model has some inherent limitations in conventional LES and these limitations remain in effect in the LBE-LES approach. Thus, for high Re flows, the lattice resolution has to be considerable since the algebraic model requires that nearly all of the inertial range is resolved. The alternate one-equation model[18] has the ability to deal with high-Re flows on relatively coarse grid and therefore, is being implemented for future studies.

Finally, it is worth noting that this type of closure also has some fundamental limitation in the LBE context since it is based on a model in the physical space, whereas the LBE simulation is in the phase space. A proper subgrid representation for the LBE-LES will require a closure model in the phase space to model the subgrid component of the collision integral. Such an approach still remains to be demonstrated.

2.3 LBE-FV coupling

The two methods, LBE-LES and FV-LES have to be coupled together with full two-way interactions in order to solve the problem. Here we achieve this coupling via boundary conditions whereby, the outflow of one (e.g., LBE) serves as inflow for the other (e.g., FV-LES) and vice-versa. In the present study, we are primarily interested in micro-blowing and therefore,

this allows us to use some simplifications. Since the diameter of the micro holes is very small (0.5 mm) and the flow rate is also very small, we assume that the flow out of these holes is controlled by the pressure in the outer domain. Thus, when the pressure is low above the holes (relative to the pressure inside the injectors, which is determined primarily by the stagnation pressure in the injection system) then there will be outflow. On the other hand, if the pressure is higher than the exit pressure of the injector then outflow will stop and there will be no net flux. For a general purpose coupling we should allow for suction (or inflow into the injectors) to occur in the latter case and this is an issue currently under study. However, for the current application this approach is considered reasonable as a first attempt to couple the two methods.

To provide "inflow" boundary conditions for the FV-LES (which is compressible solver) one variable must be specified from inside the FV domain while four can be prescribed (and one determined by equation of state). In the present implementation, temperature at the "inflow" plane is prescribed from inside the FV domain (by simple extrapolation) while density and the three velocity components are obtained from the LBE-LES solution from Eqs.12 and 13. Finally, pressure is computed using equation of state. This approach is slightly different from the approach developed for compressible inflow, as described by Poinsot and Lele,[33] where velocities and temperature are prescribed and density is computed from the backward characteristic. We plan to revisit this issue in the near future.

To provide the "outflow" boundary conditions for the LBE-LES one needs to prescribe all the distribution functions f_α. Some of these can be determined from the FV-LES input and some can be determined from inside the LBE-LES domain (see Fig. 1 for the lattice directions). In the present study, the pressure at the exit plane of the LBE domain is obtained from the FV domain (assuming zero normal pressure gradient). Then, the density is computed using $p = c_s^2 \rho$. The three velocity components at the exit plane are also given from the FV-LES domain (see additional comments below) and then, we need to solve six equations in Eq.12 and Eq.13 along with two symmetry equations:

$$f_{12} + f_{13} = f_{11} + f_{14},$$

and

$$f_{16} + f_{17} = f_{15} + f_{18}.$$

There are 8 unknown f_α that have to be prescribed. The six unknowns are determined using the five lattice outward links (i.e. 6, 12, 13, 17 and 18, see Fig.1) and the velocity component in the outflow direction. Remaining two unknown f_α are obtained by using the other two velocity components.

The above noted coupling is spatial in nature but since temporal accuracy is needed, this coupling occurs at the proper instant in time. Here, the time scale for LBE-LES is obtained by using the characteristic scale of the injector diameter and c. This time scale is compared to the characteristic time scale for the FV-LES evolution (which is the classical CFL time-step). Both solvers evolve at their individual time steps and couple at the appropriate epoch. In the present study, the LBE-LES time step is smaller than the FV-LES and thus, the LBE field can evolve longer than the FV-LES before they need to be coupled.

3 Numerical Implementation

Both the FV-LES and LBE-LES solvers are implemented in parallel using MPI library, and are highly optimized.[34] Domain decomposition is employed in both the solvers to achieve proper load balancing. In order to couple the two parallel codes, different MPI groups are defined. Thus, the two codes are parallelized and implemented independently and they are coupled through a driver code using message passing. This approach allows independent control of both solvers and makes it very easy to use LBE-LES in many injector holes without requiring major code revision. Therefore, extension of this approach to many hundreds of injectors will not be a major issue (other than the computational cost).

4 Results and Discussion

Here, we discuss the coupled simulation of a single jet in crossflow first to validate the coupled approach and then discuss its application to the MBT case.

4.1 Single Jet in Crossflow

In this study, the experiment of Ajersch *et al.*[35] is chosen as the benchmark case for validation. The dimensions of the computational domain are shown in Fig. 2. The simulation is carried out at Reynolds number of 4700 (based on the jet velocity and the nozzle width D) and at a jet-cross-flow velocity ratio of 0.5. The cross-flow velocity profile is initialized with a boundary layer thickness of $5D$. The computational domain is resolved using $128 \times 96 \times 64$ for the cross-flow domain (FV-LES) and $20 \times 20 \times 100$ for jet section (LBE). So a total of 0.82×10^6 grid points is used to discretize the complete domain. The results from these simulations are compared with the earlier results obtained using the LBE-LES for the *entire* domain.[10]

Computation of a full simulation requires approximately 1155 single-processor hours with 1.5GB memory on the IBM SP4 machine. Periodic boundaries are used in the cross-stream boundaries of the cross-flow domain to simulate a single square jet out of a row of six used in the experiment. On the top surface, slip boundary conditions are employed. Characteristic based inflow and outflow are employed for the crossflow (which is computed using the compressible FV-LES approach). For the jet, a parabolic velocity

profile is prescribed in the pipe at a distance of 5D below the flat plate allowing the flow to develop naturally as the jet merges into the cross-flow.

Results are compared with the experiment of Ajersch and numerical results with whole domain simulated using LBE-LES simulation. Comparison of LBE-LES with numerical results of Hoda *et al*[36] were discussed earlier[10] and it was shown that the full LBE-LES approach can capture with reasonable accuracy the experimental mean and rms velocity profiles. Therefore, we compare the current LBE-FV-LES coupled results against the earlier LBE-LES results.

All the important features in JICF such as the horseshoe (or kidney-shaped) structure and counter rotating vortex pair (CRVP) observed in earlier LBE-LES (and in the experiments) are captured in the present simulation with reasonable accuracy (and in very good agreement with the previous study). Figure 3 shows how the jet is turned by the crossflow and creates the kidney shaped vortices that are shed in the downstream direction.

The velocity vector field in Fig.4 shows the formation of the recirculation zone behind the jet. By reviewing time evolution of the flow field it is seen that the recirculation bubble periodically sheds the flow inphase with the motion of the kidney-shaped vortices observed in this flow (Fig. 3). The periodic shedding of the flow from the recirculation zone is show more clearly in Fig. 5 which shows the velocity contours along stream-wise direction. Smooth transition of velocity contours from LBE domain to FV domain shown in this figure clearly demonstrated the accuracy of the LBE-FV coupling employed in the present approach.

The mean stream-wise velocity profile comparison with past LBE-LES and experimental data at representative stream-wise stations ($x/D = 0, 1$) along the jet center plane ($y/D = 0$) and along the edge of the jet ($y/D = -0.5$) are shown in Figs.6 and 7. The exit plane velocity is well captured by LBE-LES and the reverse flow at $x/D = 1$ is also captured, albeit smaller in size. Further downstream the boundary reattach and continues to grow. Since there is no direct interaction between jet and cross-flow at the edges, cross-flow deflection is less compared to the deflection at the center plane. Reverse flow is not seen at this plane and this agrees with experimental data.

Turbulent kinetic energy (TKE) profiles at the jet center plane are shown in Fig.8. According to Hoda *et al*,[36] TKE is produced not only during interaction between the crossflow boundary layer and the jet but also due to various velocity gradients and strong streamline curvature. Peak of TKE profile is located at the same location of maximum velocity gradients. TKE is larger at the top of the jet where the interactions are dominant.

Finally, comparison of turbulence fluctuation intensity (Figs. 9 and 10) in the stream-wise (u_{rms}/W_j) and wall-normal (w_{rms}/W_j) directions show that these fluctuation levels are similar in magnitude but that there are significant anisotropy in the near-wall region. This is to be expected since in this region vortical breakdown occurs in a complex 3D manner.

4.2 Multiple Micro-Jets in Cross-flow

In the micro blowing technique experimentally investigated at NASA/GRC,[4] a plate with porosity of 13 to 43 percent was studied and it was shown that drag can be significantly reduced. Holes diameters ranged from around 0.2 to 0.5 millimeter and depending on plate porosity, an order of 100000 micro holes existed on a $100cm^2$ flat plate area. Simulation of flow inside such tiny holes along with a cross-flow domain whose length scale is orders of magnitude larger is a challenging problem. Here, we demonstrate the coupled LBE-FV approach for a limited set of holes but we believe that this approach can be extended to simulate a large set of holes simultaneously.

Here, we simulate a 3 x 3 square pattern of injection holes each with diameter of $D = 0.5mm$ and equally spaced a distance of D apart, as shown in Fig.11. Turbulent inflow profile is specified $5D$ upstream of injection holes with a free stream velocity of $U_0 = 138.54m/s$ and boundary layer thickness of $\delta = 12mm$. These conditions closely approximate the experimental data. Slip boundary conditions on the upper plane a distance $12D$ above the injection holes, and characteristic outflow conditions were imposed at a location $10D$ downstream of the holes. Periodic boundary conditions are imposed in the spanwise direction.

The plate porosity, as defined by cumulative hole area divide plate area, for our test case here is 25%. Two blowing rates (V_{jet}/U_0)) of 0.02 and 0.07 are simulated. The holes have an aspect ratio (L/D) of 4 and the hole inflow velocity profile has been specified as:

$$V_{inflow} = V_{jet} sin(\frac{\pi x}{D}) sin(\frac{\pi y}{D}).$$

Figure 12 shows the boundary layer profile at different stream-wise locations along the plate in-between the injection holes. It is clear that as we go downstream past the injection holes, the boundary layer detaches from surface. Friction velocity variation along the plate is shown in Fig.13. Since the injection starts at $x/D = 5$, the friction velocity decreases past this location, and once the injection stops (at $x/D = 11$), it begins to recover to its original value. This is in good agreement with experimental observation.

Figure 14 shows the comparison of the experiment profile at the inflow with the current inflow profile. It also shows the velocity profile at the injection port. As we can see, since the friction velocity goes down due to injection, higher U^+ is achieved, as expected.

Velocity vector field in the center plane for the three injection holes are shown in Fig.15. In the microblow-

ing approach, the flow from the injectors is very small and with a very small velocity. Thus, these jets interact with the viscous sublayer and the buffer layer of the incoming crossflow boundary layer. Analysis shows that the interaction is limited to a region up to $y^+ = 19$. It can be seen from this figure that whereas the jet from the leading injector penetrates further into the crossflow, the jets in its shadow have weaker impact and this shadow effect increases for the third injector. Further analysis shows that there is a complex interaction between the various injectors. Results suggest that the wake effect of the leading injector can change the local pressure above the injectors behind it and can cause periodic reduction of the mass flow. More detailed analysis is still needed to fully understand the dynamics of this interaction process as a function of the injection pressure.

3D visualization of the coherent structures in the near-wall region is shown in Fig.16 in the $y^+ = 4 - 19$ region. The flow is highly modulated by the presence of the micro injection and only further downstream do we see the formation of more turbulent mixed flow.

Spanwise-averaged normalized coefficient of friction in stream-wise direction for two different injection ratio of 0.02 and 0.07 and shown in Fig.17. As observed in the experiments[4] we also observe a significant drop in skin friction drag by up to 50 percent in the immediate vicinity of the injectors.

4.3 Pressure based multihole injection

The study discussed in the above section was limited to a small region of the flat plate with a 3 x 3 matrix of holes. As noted earlier, we are eventually interested in simulating hundreds of such holes. As a first step towards this goal, we investigate pressure based injection condition over a much large 4 x 6 matrix of microholes. In this approach, the flow inside the holes are not resolved and the holes themselves are not resolved. Rather, injection conditions are imposed on the chosen grid points on the flat plate by assigning the wall normal velocity component to be proportional to the pressure fluctuation at the injection port, whereas the two other velocity components are assumed to be zero.

For this case, the Reynolds number, based on the channel half width ($h = 0.071$) and the bulk velocity of 138.5468 is 630,534. A grid of $64 \times 148 \times 64$ is used to resolve the computational domain as shown in Fig.18. Uniform grid is used in the streamwise (x) and spanwise directions (z) and a stretched grid is employed in the wall normal direction (y). Cross symbols in Fig.18 show the injection points and domain dimensions are given in meter. Periodic boundary condition are imposed in the span-wise direction and no-slip boundary condition at both walls are imposed.

The skin friction coefficient for this simulation is given in Fig. 19. It is obvious that pressure fluctuations decreases the mean shear and thus, the skin friction. This simple study suggests that scaleup of the coupled LBE-FV to many holes should also result in similar drag reduction. We plan to explore this in the near future.

5 Conclusions

In this paper, 3D LES of single and multiple jet-in-cross-flow (JICF) are conducted using the 19-bit Lattice Boltzmann Equation (LBE) method coupled with a conventional finite-volume (FV) scheme. In this coupled LBE-FV approach, the LBE-LES is employed to simulate the flow inside the jet nozzles while the FV-LES is used to simulate the crossflow. The key application area is the use of this technique is to study the micro blowing technique (MBT) for drag control similar to the recent experiments at NASA/GRC. It is necessary to resolve the flow inside the micro-blowing and suction holes with high resolution without being restricted by the FV time-step restriction. The coupled LBE-FV-LES approach achieves this objectives in a computationally efficient manner.

The single jet in crossflow case is used for validation purpose and the results are compared with experimental data and full LBE-LES simulation. Good agreement with data is obtained. Subsequently, MBT over a flat plate with porosity of 25% is simulated using 9 jets (in a 3 x 3 matrix) in a compressible cross flow at a Mach number of 0.4. Two cases with injection ratios of 0.02 and 0.07 are conducted to investigate how the blowing rate impacts skin friction. It is shown that MBT suppresses the near-wall vortices and modifies the near-wall sweep-burst events. This in turn reduces the skin friction drag; a reduction up to 50 percent in the vicinity of the injectors is seen in the present study. This is in good agreement with experimental data. Future studies will address the fully coupled simulation of a much larger matrix of injectors to understand the interaction between the multiple jets and the issue of scalability of this drag reduction method.

6 Acknowledgement

This work is supported in part by Army Research Office and NASA Glenn Research Center. Computational time was provided by Department of Defense High Performance Computing Centers at ERDC (MS) and NAVO (MS).

References

[1] Hwang, D., "A proof of concept experiment for reducing skin friction by using a Micro-Blowing Technique," *AIAA-97-0546 (NASA TM 107315)*, 1997.

[2] Hwang, D. P. and Biesiadny, T. J., "Experimental evaluation of the penalty associated with micro-blowing for reducing skin friction," *NASA TM 113174*, 1997.

[3] Hwang, D. P., "Skin friction reduction by a microblowing technique," *AIAA J.*, Vol. 36, 1998, pp. 480–481.

[4] Hwang, P. D., "Experimental study of characteristics of micro-hole porous skins for turbulent skin friction reduction," *ICAS 2002 CONGRESS*, 2002.

[5] Welch, G. E., Larosiliere, L. M., Hwang, D. P., and Wood, J. R., "Effectiveness of micro-blowing technique in adverse pressure gradients," *AIAA Paper No. 2001-1012*, 2001.

[6] Lin, Y. L., Chyu, M. K., Shih, T. P., Willis, B. P., and Hwang, D. P., "Skin friction reduction through Micro-Blowing," *AIAA Paper No. 98-0359, 36th Aerospace Sciences Meeting, Reno, NV.*, 1998.

[7] Menon, S., "Computational modeling of MEMS-based micro-jets to Control supersonic boundary layers," *Computational Combustion Laboratory Technical Report CCL-99-002, Georgia Tech., April 1999*, 1999.

[8] Kemenov, K. and Menon, S., "TLS: A new two-level simulation methodology for high-Re LES," *AIAA Paper 2002-0287*, 2002.

[9] Wang, H. and Menon, S., "Fuel-air mixing enhancement by synthetic microjets," *AIAA Journal*, Vol. 39, No. 12, 2001, pp. 2308–2319.

[10] Feiz, H., Soo, J. H., and Menon, S., "LES of Turbulent jets using the lattice Boltzmann approach," *AIAA Paper 03-0780*, 2003.

[11] Nelson, C. C. and Menon, S., "Unsteady simulations of compressible spatial mixing layers," *AIAA-98-0786*, 1998.

[12] Patal, N. and Menon, S., "Large-Eddy Simulation of turbulent flow over an axisymmetric hill," *AIAA Paper 2003-0967*, 2003.

[13] Kim, W.-W., Menon, S., and Mongia, H. C., "Large eddy simulations of a gas turbine combustor flow," *Combustion Science and Technology*, Vol. 143, 1999, pp. 25–62.

[14] Kim, W.-W. and Menon, S., "Numerical modeling of turbulent premixed flames in the thin-reaction-zones regime," *Combustion Science and Technology*, Vol. 160, 2000, pp. 110–150.

[15] Menon, S., "Subgrid combustion modelling for LES of single and two-phase reacting flows," *Advances in LES of Complex Flows*, 2000, pp. 329–352.

[16] Erlebacher, G., Hussaini, M. Y., Speziale, C. G., and Zang, T. A., "Toward the Large-Eddy Simulation of compressible turbulent flows," *Journal of Fluid Mechanics*, Vol. 238, 1992, pp. 155–185.

[17] Schumann, U., "Subgrid scale model for finite difference simulations of turbulent flows in plane channels and annuli." *Journal of Computational Physics*, Vol. 18, 1975, pp. 376–404.

[18] Kim, W.-W. and Menon, S., "A new incompressible solver for large-eddy simulations," *International Journal of Numerical Methods in Fluids*, Vol. 31, 1999, pp. 983–1017.

[19] Menon, S. and Kim, W.-W., "High Reynolds number flow simulations using the localized dynamic subgrid-scale model," *AIAA Paper 96–0425*, 1996.

[20] Menon, S., Yeung, P.-K., and Kim, W.-W., "Effect of subgrid models on the computed interscale energy transfer in isotropic turbulence," *Computers and Fluids*, Vol. 25, No. 2, 1996, pp. 165–186.

[21] Liu, S., Meneveau, C., and Katz, J., "On the properties of similarity subgrid-scale models as deduced from measurements in a turbulent jet," *Journal of Fluid Mechanics*, Vol. 275, 1994, pp. 83–119.

[22] Germano, M., Piomelli, U., Moin, P., and Cabot, W., "A dynamic subgrid-scale eddy viscosity model," *Physics of Fluids A*, Vol. 3, No. 11, 1991, pp. 1760–1765.

[23] Schumann, U., "Realizability of Reynolds-stress turbulence models," *Physics of Fluids*, Vol. 20, No. 5, 1977, pp. 721–725.

[24] Chen, H., Chen, S., and Matthaeus, W., "Recovery of the Navier-Stokes equations using a lattice-gas Boltzmann method," *Physical Review A*, Vol. 45, 1992, pp. 5339–5342.

[25] Qian, Y., d'Humierès, D., and Lallemand, P., "Lattice BGK models for the Navier-Stokes equation," *Europhysics Letters*, Vol. 17, 1992, pp. 479–484.

[26] Bhatnagar, P., Gross, E., and Krook, M., "A model for collision process in gases. I. Small amplitude process in charged and neutral one-component system," *Physical Review A*, Vol. 94, 1954, pp. 551–525.

[27] Chen, S. and Doolen, D., "Lattice Boltzmann method for fluid flows," *Annual Review of Fluid Mechanics*, Vol. 30, 1998, pp. 329–364.

[28] Grunau, D., Chen, S., and Eggert, K., "A lattice Boltzmann model for multiphase fluid flows," *Physics of Fluids A*, Vol. 5, 1993, pp. 2557–2562.

[29] Frisch, U., Hasslacher, B., and Pomeau, Y., "Lattice-gas automata for the Navier-Stokes equations," *Physical Review Letters*, Vol. 56, 1986, pp. 1505–1508.

[30] Qian, Y., S., S., and Orszag, S., "Recent advances in lattice Boltzmann computing, In Stauffer, D., editor," *Annual reviews of computational physics III*, 1995, pp. 195–242.

[31] Mei, R., Shyy, W., Yu, D., and Luo, L., "Lattice Boltzmann method for 3D flows with curved boundary," *Journal of Computational Physics*, Vol. 161, 2000, pp. 680–699.

[32] Kim, W.-W., Menon, S., and Mongia, H., "Numerical simulations of reacting flows in a gas turbine combustor," *Combustion Science and Technology*, Vol. 143, 1999, pp. 25–62.

[33] Poinsot, T. J. and Lele, S. K., "Boundary conditions for direct simulation of compressible viscous flows," *Journal of Computational Physics*, Vol. 101, 1992, pp. 104–129.

[34] Stone, C. and Menon, S., "Parallel simulations of swirling turbulent flames," *Journal of Supercomputing*, Vol. 22, 2002, pp. 7–28.

[35] Ajresch, P., Zho, J., Ketler, S., Salcudean, M., and Gartshore, I., "Multiple jets in a crossflow: detailed measurments and numerical simulations," *Journal of Turbomachinery*, Vol. 119, 1997, pp. 330–342.

[36] Hoda, A., Acharya, S., and Tyagi, M., "Reynolds strees transport model predictions and large eddy simulations for film coolant jet in crossflow," *Proceedings of ASME TURBOEXPO 2000*, 2000, pp. 1–15.

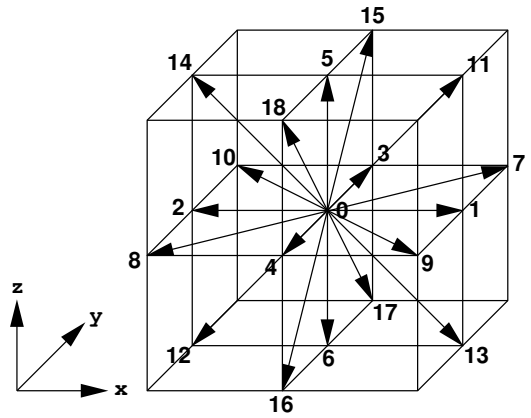

Fig. 1 Link vectors of f_α.

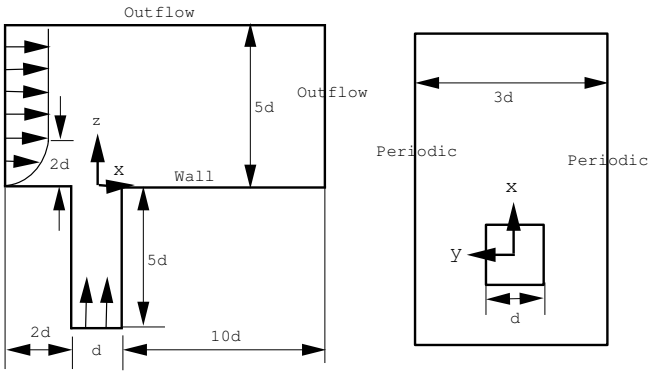

Fig. 2 Geometry and computational domain for the single jet in crossflow.

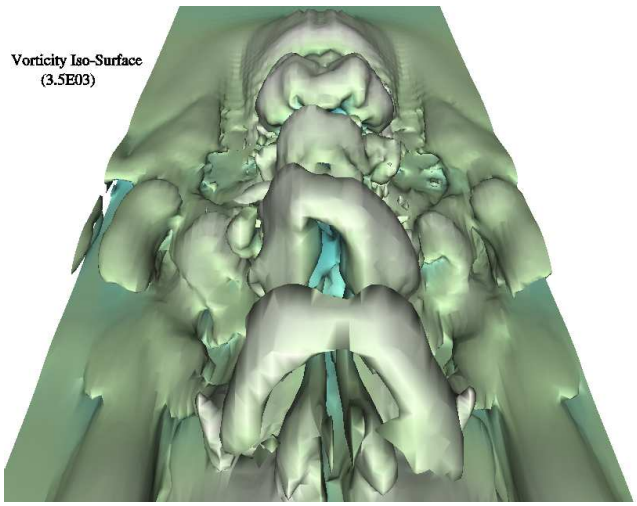

Fig. 3 Vorticity iso-surface for the JICF shows the formation and motion of the kidney-shaped vortices.

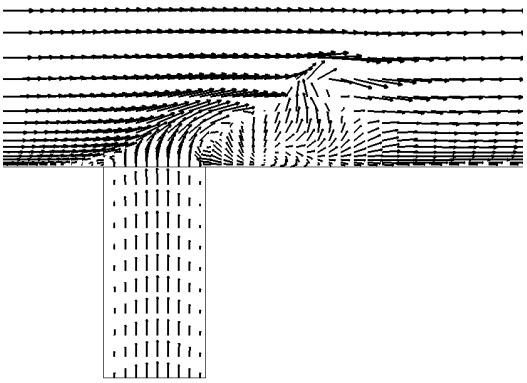

Fig. 4 Velocity vector field shows the formation of the recirculation zone in the shadow of the jet.

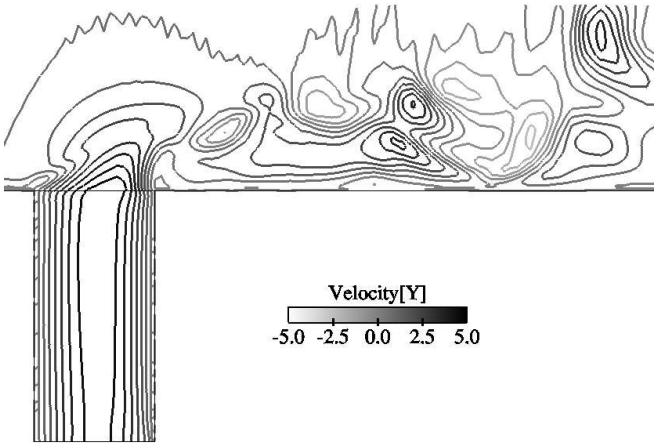

Fig. 5 Velocity contours shows the flow in the recirculation zone and the motion downstream.

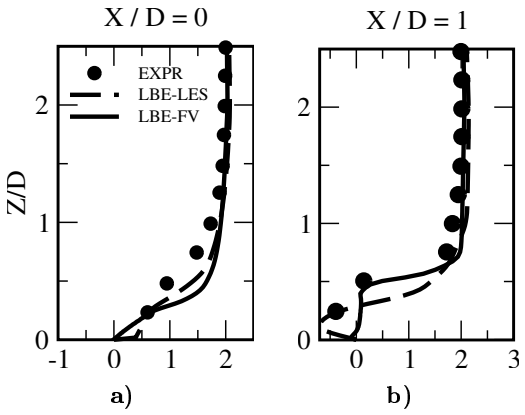

Fig. 6 Mean stream-wise velocity profiles (U/W_j)along the jet center plane (y/D=0) at x/D=0,1 from the jet center.

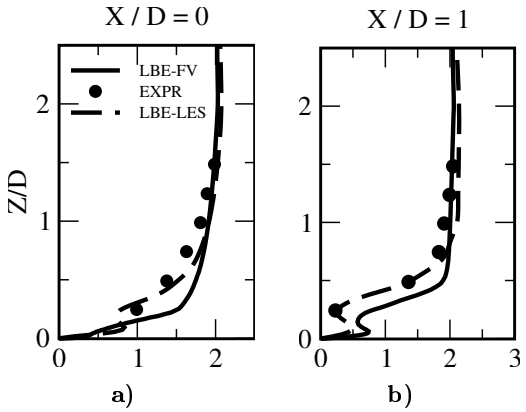

Fig. 7 Mean stream-wise velocity profiles (U/W_j)along the jet edge plane (y/D=-0.5) at x/D=0,1 from the jet center.

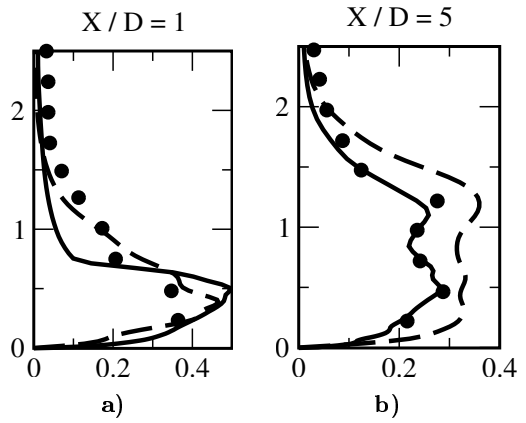

Fig. 8 Mean turbulence kinetic energy $\sqrt{k}/W_j$ along the jet center plane (y/D=0) at x/D=1,5 from the jet center.

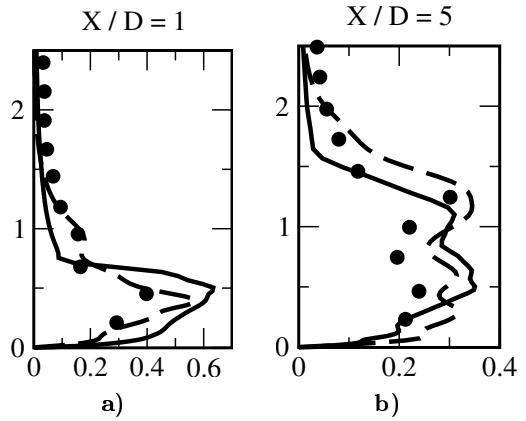

Fig. 9 Stream-wise fluctuation u/W_j^2 profiles along the jet edge plane (y/D=0) at x/D=1,5 from the jet center.

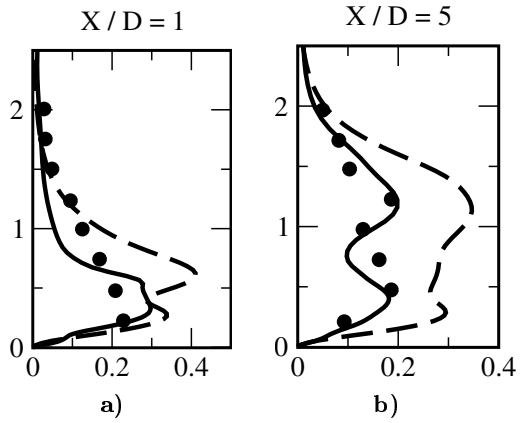

Fig. 10 Normal fluctuation w/W_j^2 profiles along the jet edge plane (y/D=0) at x/D=1,5 from the jet center.

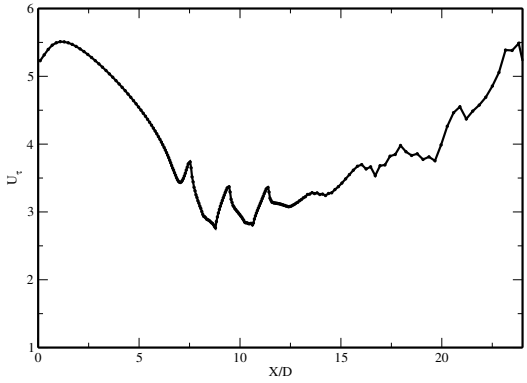

Fig. 13 Spanwise-averaged normalized friction velocity in stream-wise direction.

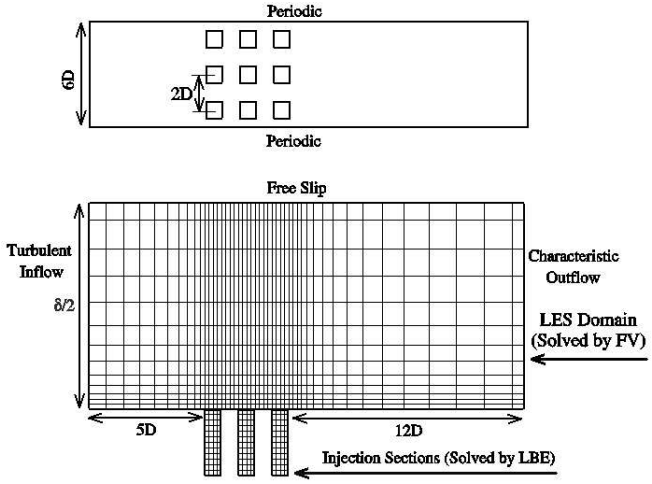

Fig. 11 Geometry and grid configuration for multi hole simulation (every five grid is shown).

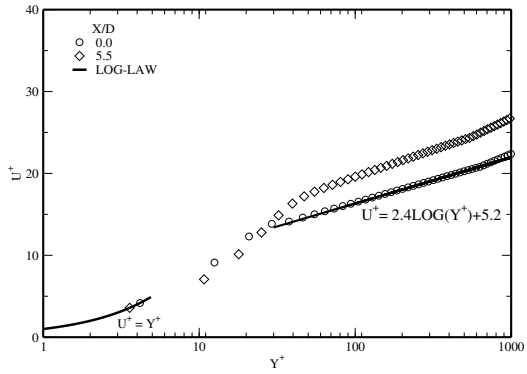

Fig. 14 U^+ velocity profile in the wall coordinate Y^+

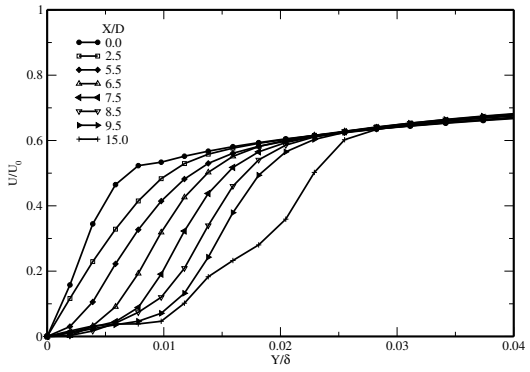

Fig. 12 Boundary layer profile along the jet plane (y/D=0) at different x/D.

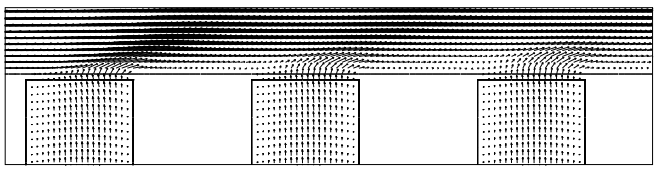

Fig. 15 Velocity field in the center place of the three injectors. The shadow effect of the leading injector is seen on the injectors behind it.

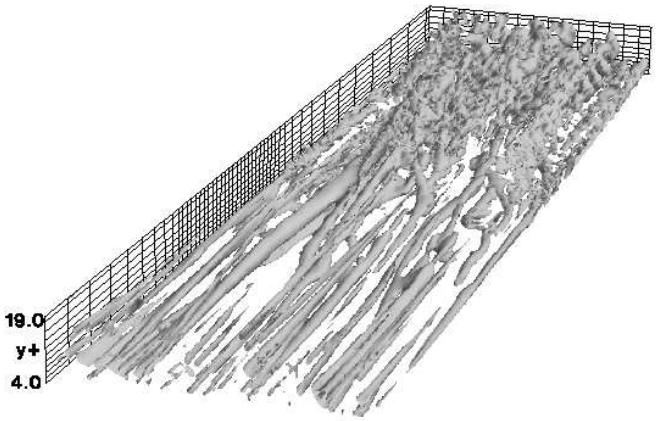

Fig. 16 Coherent structures in the near-wall region

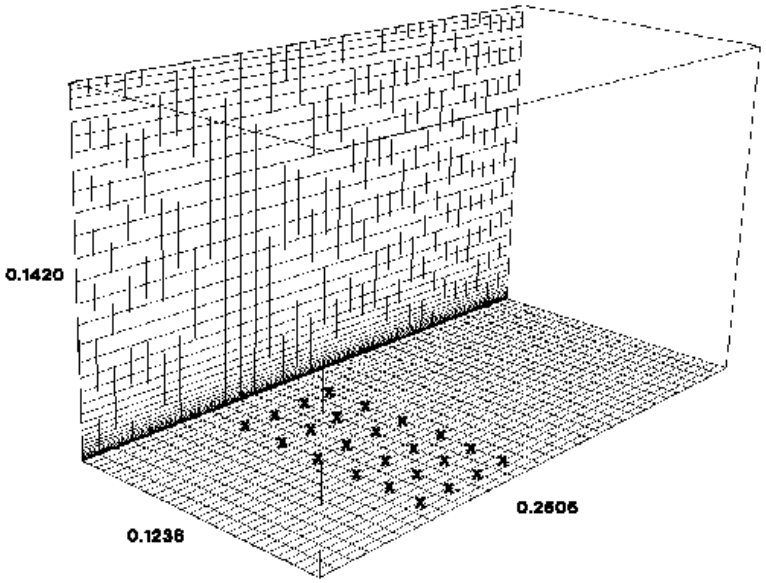

Fig. 18 Geometry for the multi-hole injection study.

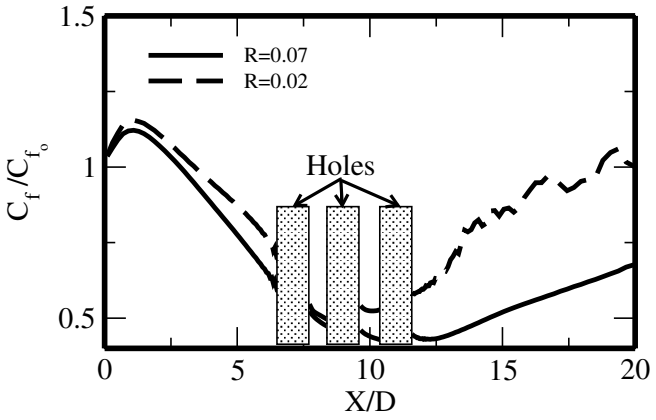

Fig. 17 Coefficient of friction along the plate for different injection ratio.

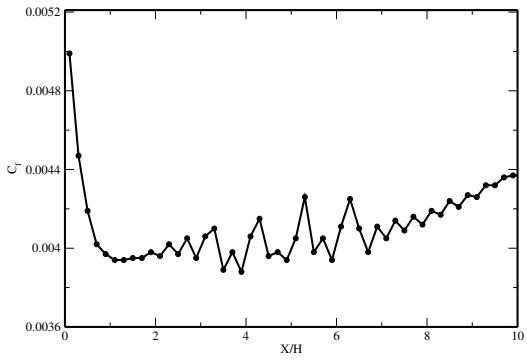

Fig. 19 Coefficient of friction variation in the streamwise direction for the multihole injection.